RESEARCH ARTICLE | MARCH 19 2025

Combined electron cyclotron resonance and radio frequency discharges in the TOMAS facility

Yu. Kovtun ; T. Wauters ; A. Goriaev ; L. Dittrich ; L. D. López-Rodríguez ; K. Crombé ; S. Moon ; P. Petersson ; J. Buermans ; S. Möller ; S. Brezinsek

Phys. Plasmas 32, 032512 (2025)
https://doi.org/10.1063/5.0247996

Combined electron cyclotron resonance and radio frequency discharges in the TOMAS facility

Cite as: Phys. Plasmas **32**, 032512 (2025); doi: 10.1063/5.0247996
Submitted: 9 November 2024 · Accepted: 27 February 2025 ·
Published Online: 19 March 2025

View Online Export Citation CrossMark

Yu. Kovtun,[1,a)] T. Wauters,[2] A. Goriaev,[3] L. Dittrich,[4] L. D. López-Rodríguez,[3,5] K. Crombé,[3,5] S. Moon,[2] P. Petersson,[4] J. Buermans,[3,5] S. Möller,[6] and S. Brezinsek[6]

AFFILIATIONS

[1]Institute of Plasma Physics, National Science Center Kharkiv Institute of Physics and Technology, 61108 Kharkiv, Ukraine
[2]ITER Organization, CS 90046, 13067 St. Paul-lez-Durance, France
[3]Laboratory for Plasma Physics, LPP-ERM/KMS, 1000 Brussels, Belgium
[4]Fusion Plasma Physics, KTH Royal Institute of Technology, 10044 Stockholm, Sweden
[5]Department of Applied Physics, Ghent University, 9000 Ghent, Belgium
[6]Institute for Energy and Climate Research – Plasma Physics, Forschungszentrum Jülich GmbH, 52428 Jülich, Germany

[a)]**Author to whom correspondence should be addressed:** Ykovtun@kipt.kharkov.ua

ABSTRACT

The experiments carried out in hydrogen at the TOMAS facility show the possibility of controlling plasma parameters such as temperature and electron density in a combined electron cyclotron resonance and radio frequency (ECR+RF) discharge. A maximum plasma density of up to $\approx 6 \times 10^{16}$ m^{-3} and electron temperature of up to 35 eV are observed in the combined ECR+RF discharge. The propagation of RF waves in hydrogen plasma under a weak magnetic field is analyzed. Depending on RF frequency and experimental conditions, such as radial distribution of plasma density and magnetic field, there can be several cases: only the slow wave can propagate, simultaneously slow and fast waves can propagate, or only the fast wave can propagate. The injection of additional RF power into the ECR discharge allows us to change the flux of neutral particles and their distribution function. Even the injection of small RF power of ≈ 0.26 kW relative to microwave power of ≈ 1.7 kW leads to an increase in the hydrogen flux by a factor of ~2.5. At RF power $P_{RF} \approx 1.57$ kW, the H^0 flux increases by a factor of ~9.3. The ability to control the fluxes and energies of particles leaving the plasma volume is important to approach the conditions necessary to study plasma–surface interactions in wall conditioning and fusion edge plasmas.

I. INTRODUCTION

High-frequency methods in the range of electron cyclotron resonance (ECR) and ion cyclotron resonance (ICR) and their harmonics are used to produce and heat plasma in magnetically confined toroidal devices for controlled fusion.[1–5] Also, high-frequency methods are used to produce plasma for wall conditioning procedures.[6,7]

For the realization of ICR discharges during ion cyclotron wall conditioning (ICWC), the same radio frequency (RF) systems are used as for ICR heating.[8,9] In tokamaks and stellarators, RF discharges at frequencies significantly higher than the ion cyclotron frequency $\omega_{RF} \gg \omega_{ci}$ are also used for wall conditioning.[10–15] At the same time, RF systems designed for ICR heating can be used to realize such RF discharges, and there is no need to change the RF frequency. The magnitude of the magnetic field required for plasma production by RF waves can be very small.[14,15]

For the realization of ECR discharges, including electron cyclotron wall conditioning (ECWC), the presence of a cyclotron zone in the plasma column, where the resonance condition $\omega_{MW} = n\omega_{ce}$ (n are the harmonic numbers) for the fundamental frequency and its harmonics are satisfied, is a necessary condition. Therefore, ECR systems can only produce plasma in the same magnetic field range as used for ECR heating. For example, at the Wendelstein 7-X stellarator, the ECR system at 140 GHz is used both for plasma generation and heating[3] and for ECWC in a magnetic field of 2.5 T.[16,17] In the case of significant decrease in magnetic field for ECWC discharges, it is necessary to use ECR system with another frequency. ECWC discharges with a frequency of 2.45 GHz are studied and used.[18–21] The 2.45 GHz frequency is standard in many plasma technologies.[22] Note that the production of plasma at 2.45 GHz is also possible under the condition $\omega_{ce}/\omega_{MW} > 1$.[23] Such a plasma was used earlier as a target plasma for

subsequent heating during neutral beam injection in Heliotron J.[24–26] This type of discharge has also been investigated previously at stellarators WEGA[27] and TJ-K.[28]

Previously, the combination of ECR and ICR discharges was used for the wall conditioning process in the TEXTOR-94 tokamak.[29,30] In applied plasma technologies, the combination of ECR at 2.45 GHz and RF discharges is used.[31–34] Typically, these discharges use a substrate as an electrode, biased by the RF power source relative to the chamber wall.

The study of combined ECR+RF discharge was performed on a TOMAS toroidal device.[35–38] In these studies, the plasma was produced and maintained by ECR discharge at the frequency of 2.45 GHz with additional RF power injected, or the combined ECR+RF discharge was realized. The first studies of helium plasma showed that the addition of RF power at 25 MHz to the plasma supported by the ECR discharge allowed to increase the electron temperature and density to extend the range of these parameters at a given gas flow.[35] Thus, it is possible to change the plasma parameters independently of the ECR discharge. The first experiments to determine the fluxes of low energy hydrogen atoms from hydrogen plasma showed that the flux of neutral atoms and their temperature were higher in the combined ECR+RF discharge than in the ECR itself.[36] In Ref. 37, the plasma parameters of ECR and combined ECR+RF discharges of the first hydrogen experiments at TOMAS were analyzed and compared.

The present work is a continuation of the studies of the combined ECR+RF discharge started earlier in Refs. 35–38. The main goal is to study the parameters of ECR+RF discharges in hydrogen, as well as the flux of neutral hydrogen atoms from the plasma of ECR+RF discharge depending on the RF power. The study of such a discharge is of interest for wall conditioning methods and providing conditions that allow the study of fusion edge plasma in the scrape-off layer.[39]

II. EXPERIMENTAL SETUP AND DIAGNOSTICS

The combined ECR+RF discharge was studied on the TOroidal MAgnetized System (TOMAS) at Forschungszentrum Jülich, Germany,[40,41] the schematic view of which is shown in Fig. 1. The TOMAS device is a simple magnetized torus. The main technical parameters are presented in Table I. The vacuum system is described in detail in Ref. 41.

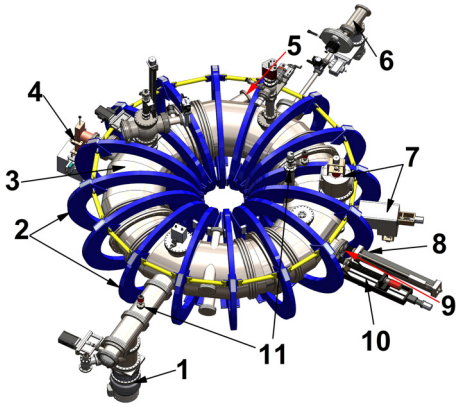

FIG. 1. Scheme of the TOMAS device. Turbopump (1), toroidal coils (2), vacuum vessel (3), microwave heating system (4), location of the video diagnostics and gas puffing (5), time-of-flight neutral particle analyzer (6), radio frequency system (7), triple probe (8), optical emission spectroscopy (9), single Langmuir probe (10), and vacuum gauges (11).

The microwave heating system [see Fig. 1 position (4) and Table I] includes a microwave generator, magnetron power supply, power monitoring and oscillator protection circuit, and impedance matching circuit.[41] The output microwave power is transmitted to the vacuum volume through a circular port (diameter of 100 mm) quartz window (thickness of 6.22 mm).

The RF system includes [see Fig. 1 position (7) and Table I] the RF generator, RF solid-state amplifier, transmission coaxial feeder line of 50 Ω, matching system, single strap antenna (width of 90 mm and a thickness of 5 mm), antenna box, as well as control and diagnostics systems.[41]

The plasma diagnostics methods at TOMAS include Langmuir probes, optical diagnostics, and particle detectors.[38] Plasma density and electron temperature are measured with a symmetrical triple probe (TP).[35,38,41] The probe tips made of a tungsten cylindrical wire have a length of 4 mm and a diameter of 0.8 mm. The TP operates in voltage mode (direct-display method).[42] This mode uses two tips, 1 and 2, of the TP that are biased relative to each other, and one tip, 3, of the TP that is floating. The electron temperature is determined from voltage measurements between tips 2 and 3 of the TP. The plasma density is determined from the ion saturation current between tips 1 and 2 of the TP. The probe design and measurement methodology are described in more detail in Ref. 42. The movable TP is installed on the horizontal port of the vacuum vessel [see Fig. 1(8)]. The radial distributions of electron temperature and density are measured using a pulse-by-pulse technique (radial scanning).

To determine the elemental/charge content of plasma, the non-contact passive method of time-resolved optical emission spectroscopy (OES) of plasma was used. The line-integrated plasma spectrum of line emission [see Fig. 1 position (9)] is registered in the spectral range from 175 to 1100 nm with the fiber optic spectrometer.[38,43] The integration time is 100 ms. The spectral lines are identified according to the data from Ref. 44.

Plasma events in the vacuum chamber volume are recorded using video cameras.[38,41] The camera is installed in the tangential port [see Fig. 1 position (5)].

Measurement of neutral particle flux uses time-of-flight neutral particle analyzer (ToF NPA).[36,41] The time- and energy-resolved

TABLE I. Technical parameters of TOMAS.

Parameter	Value
Major radius (m)	0.78
Minor radius (m)	0.26
Volume (m^3)	1.1
Magnetic system	16 toroidal coils
Max B_0 (T)	0.125
RF frequency (MHz)	10–50
RF power (kW)	up to 6.0
Microwave frequency (GHz)	2.45
Microwave power (kW)	0.6–6.0

neutral particle distribution can be measured with this method. The neutral particle energy range of the system is 10–1000 eV.

Signals from the microwave and RF systems, pressure, and triple probe are collected by the Data Acquisition System (DAS) of TOMAS. The DAS is operated by LabView scripts. The RF and microwave systems are run by the Python scripts.

III. RESULTS AND DISCUSSION

A. Overview of the experiments

The experiments are performed in a hydrogen atmosphere. First, the vacuum chamber is pumped to a pressure of 1.2×10^{-5} Pa. Then, high-purity hydrogen is continuously injected into the vacuum chamber up to the required pressure. The radial distribution of the magnetic field is determined from the equation $B(r) = 5.7 \times 10^{-5} \times I_c \times (R_0/(R_0 + r))$, where I_c is the coil current, R_0 is the major radius, and r is the radial coordinate.[41] The value of the steady magnetic field at $I_c = 1.4$ kA in the center of the vacuum chamber is $B_0 \approx 0.0798$ T. The value of the magnetic field strength in the equatorial plane near the vacuum chamber wall at the High Field Side (HFS) region is $B \approx 0.12$ T ($r \approx -26$ cm), and in the Low Field Side (LFS) region, it is $B \approx 0.06$ T ($r \approx 26$ cm). The ECR region was located at the radial coordinate $r \approx -6.9$ cm ($B \approx 0.0876$ T). The RF frequencies used in the experiments are 14 and 25 MHz.

The scenario was similar to the previous experiments.[35,37] First, the plasma was produced by ECR discharge and maintained for ~2 s (see Fig. 2). Then, additional RF power was injected into the plasma for ~2 s (see Fig. 2). Thus, a combined ECR+RF discharge was realized. The initial hydrogen pressure, RF, and power were varied, while measuring the plasma density and temperature. To compare the radial distribution of plasma electron density and temperature in ECR and combined ECR+RF discharges, two quasi-stationary time windows of 1–1.5 and 2.75–3.25 s were selected (see Fig. 2). The duration of each window was 0.5 s. The average values of the plasma parameters were obtained for these windows. In a series of experiments, the flux of neutral hydrogen atoms was measured at different values of microwave power and RF power. The RF frequency for these measurements was 25 MHz.

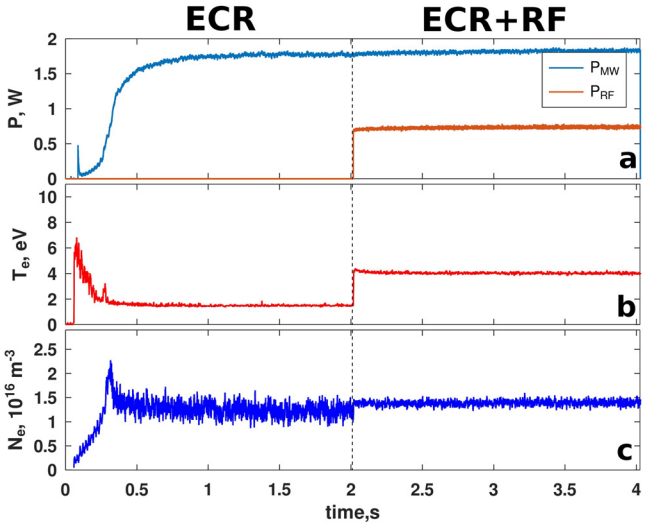

FIG. 2. Time evolution of microwave power P_{MW} and RF power P_{RF} f = 25 MHz (a), electron temperature T_e (b), electron density N_e (c) (gas: H_2, continuous gas flow Q = 35 sccm, initial pressure $p_0 = 0.13$ Pa, radial position r = −5.8 cm).

B. ECR and combined ECR+RF discharges

Figure 3 shows the time evolution of electron temperature [see Fig. 3(a)] and plasma density distributions [see Fig. 3(b)] for ECR and combined ECR+RF discharges. When microwave power is injected into the vacuum chamber, microwave breakdown and ignition of the ECR discharge occurs, which is characterized by the appearance of glow [see Fig. 4(a)] in the ECR region. A similar situation was previously observed in Ref. 38. At the initial stage of plasma production with density $<1 \times 10^{15}$ m^{-3} [see Figs. 2 and 3(b)], the maximum T_e value is observed in the ECR region [see Fig. 3(a)]. In this case, ECR is the main mechanism of electron heating. Furthermore, the plasma density increases [see Figs. 2 and 3(b)], and the maximum T_e value begins to shift radially to the LFS region [see Fig. 3(a)]. A similar picture was previously observed in the helium plasma of the ECR discharge.[35] After ~0.5 s, the ECR discharge enters the quasi-stationary phase, where the plasma parameters change slightly (see Fig. 3). Emission from the plasma is observed from the entire volume [see Fig. 4(b)]. More intense emission from the plasma is observed in the region nearer to the LFS. This is due to the higher density and temperature of the plasma, as can be seen in Fig. 3. In the line spectrum [see Fig. 5(a)], the spectral lines of the excited hydrogen atoms of the Balmer series are observed.

In the case of weak absorption of microwaves, their multiple reflection from the vacuum chamber wall occurs. This leads to multipass absorption and mixing of polarization microwave.[39,41] Various mechanisms of microwave conversion and absorption have been discussed in Refs. 1 and 45–48. Figure 6 shows the density dependence for left-hand (L) polarized wave, right-hand (R) polarized wave, and O-mode wave, above which the waves do not propagate. In these experiments in hydrogen, the plasma density was below the critical density of 7.45×10^{16} m^{-3} for the O-mode wave [see Figs. 3(b), 7(b), 8(b), and 9(b)]. Note that in previous experiments in a helium atmosphere, plasma densities up to $\approx 1.3 \times 10^{17}$ m^{-3} were achieved.[35] The value of the plasma density at which the upper hybrid resonance (UHR) condition is satisfied is shown in Fig. 6. The observed shift of the maximum T_e along the radius [see Fig. 3(a), time up to ≈0.5 s] is associated with an increase in the plasma density and, consequently, with the fulfillment of the UHR condition (see Fig. 6). This leads to an additional heating of the plasma electrons and a further increase in the plasma density. As a result, the region where the UHR condition is carried out begins to shift to the LFS region, resulting in the observed pattern of shift of the maximum T_e value.

The RF power injection into the ECR discharge plasma leads to changes in the radial distribution of temperature and plasma density (see Figs. 3 and 7–9). Moreover, the changes in T_e and N_e occur in a rather short time ~0.1 s, and after ~0.25 s, the combined ECR+RF discharge enters the quasi-stationary phase (see Figs. 2 and 3). The intensity of the spectral lines of the excited hydrogen atom increases [see Fig. 5(b)]. The change of plasma parameters at the injection of additional RF power is related to the possibility of propagation and absorption of electromagnetic waves at RF frequency in the plasma. At the same time, the conditions of microwave propagation may change, leading to a change in the dominant mechanisms of microwave

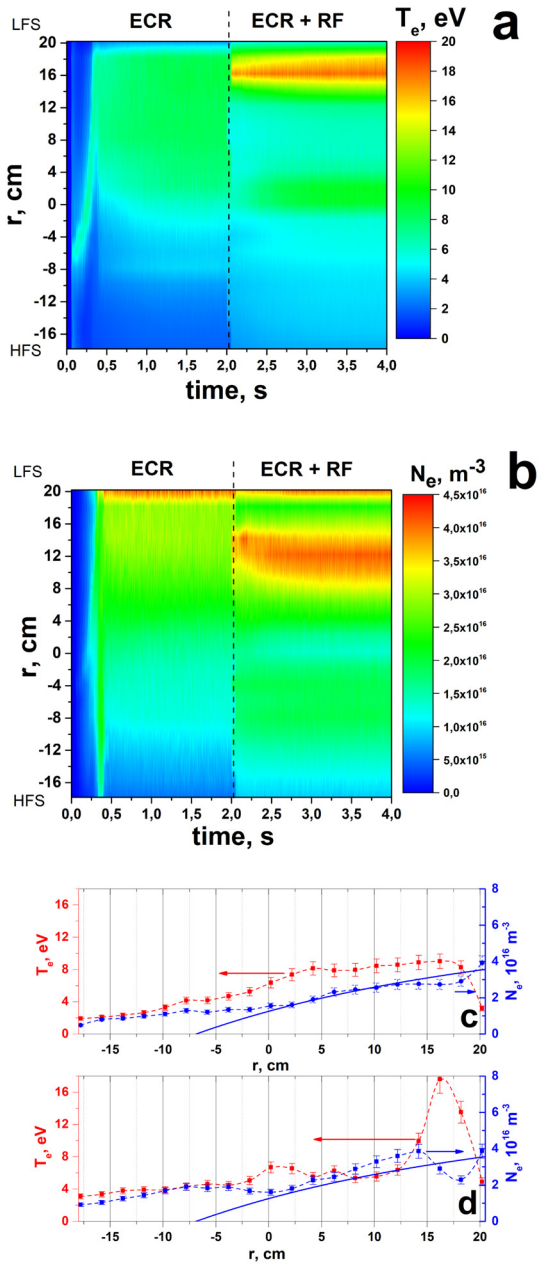

FIG. 3. Time evolution of the radial distribution of the electron temperature T_e (a) and density N_e (b). Radial distribution of electron temperature T_e and density N_e for ECR discharge at 1.75 s (c) and ECR+RF discharge at 2.25 s (d). Blue solid lines (c) and (d) indicate density necessary to fulfill of the upper hybrid resonance (UHR) condition [gas: H_2, continuous gas flow Q = 20 sccm, initial pressure $p_0 = 6.5 \times 10^{-2}$ Pa, ECR discharge $P_{MW}(max) \approx 2$ kW, combined ECR+RF discharge $P_{MW}(max) \approx 1.5$ kW, $P_{RF}(max) \approx 0.75$ kW, f = 25 MHz].

conversion and absorption in the plasma. As a result, due to changes in plasma parameters, there is an influence of both RF waves and microwaves on their propagation and absorption conditions. In some cases, this effect is clearly visible. For example, a change in the plasma

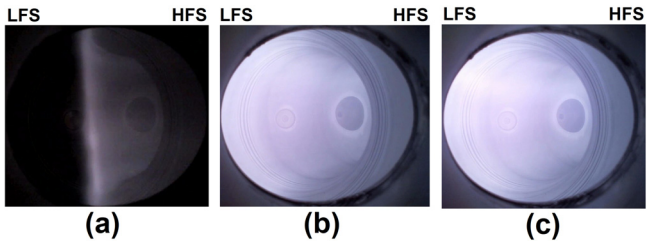

FIG. 4. The photo of ECR breakdown (a), ECR discharge (b), and combined ECR+RF discharge (c) [gas: H_2, continuous gas flow Q = 20 sccm, initial pressure $p_0 = 6 \times 10^{-2}$ Pa, ECR discharge $P_{MW}(max) \approx 1.7$ kW, combined ECR+RF discharge $P_{MW}(max) \approx 1.7$ kW, $P_{RF}(max) \approx 1$ kW, f = 25 MHz].

density may or may not lead to the fulfillment of the UHR conditions, as already discussed. This situation can be seen in Figs. 3–7. Figure 7(b) shows that an increase in the plasma density in the combined ECR+RF discharge at region r ∼ 4–12 cm leads to the fulfillment of the UHR condition. At the same time, T_e increases slightly [see Fig. 7(a)]. At r ≈ 2.4 cm, the UHR condition is satisfied for both ECR and ECR+RF discharges, and T_e does not change. In Fig. 3, the situation is somewhat different. An increase in the density around r ∼ 6–12 cm leads to the non-fulfillment of the UHR condition, and the electron temperature decreases [see Fig. 3(d)]. A similar situation has already been observed in Ref. 37.

The cases discussed are special cases, and it is not always possible to clearly see which mechanisms lead to changes in plasma parameters in ECR+RF discharge, as in Figs. 8 and 9. Obviously, the ECR discharge plasma parameters affect the propagation and absorption of RF waves for different frequencies. A qualitative comparison of Fig. 7 (f = 25 MHz, gas flow Q = 35 sccm) and Fig. 8 (f = 14 MHz, gas flow Q = 10 sccm) data shows that for the plasma and discharge parameters in the case of Fig. 7, only at r ∼ 0–4 cm, the plasma parameters do not

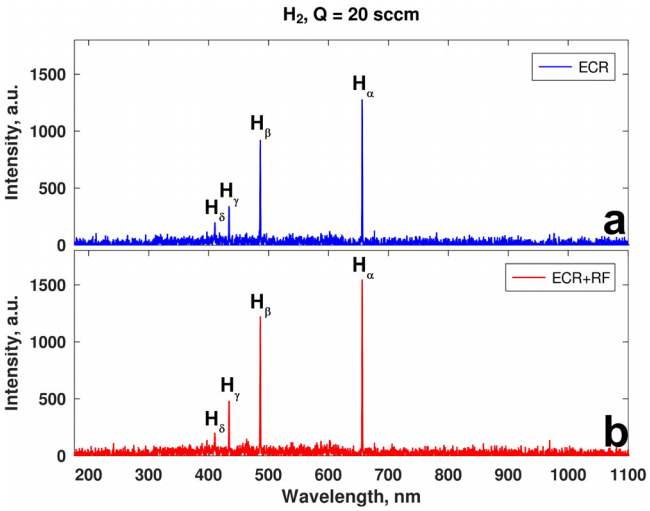

FIG. 5. Optical emission spectrum in the range of 175–1100 nm for ECR discharge (a) and combined ECR+RF discharge (b) [gas: H_2, continuous gas flow Q = 20 sccm, initial pressure $p_0 = 4.5 \times 10^{-2}$ Pa, ECR discharge $P_{MW}(max) \approx 1.2$ kW, combined ECR+RF discharge $P_{MW}(max) \approx 1.2$ kW, $P_{RF}(max) \approx 0.7$ kW, f = 25 MHz].

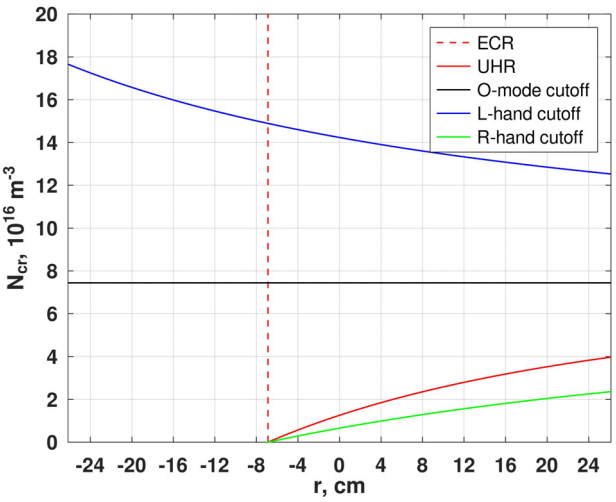

FIG. 6. Relation between position and density for cutoff densities.

change significantly. In the other two regions r ∼ −17.6–0 cm and r ∼ 4–20.3 cm, the plasma parameters change significantly. In the case shown in Fig. 8, the plasma density at r ∼ −17.6–4 cm and the temperature at r ∼ −17.6 to −8 cm do not change significantly. Although the injected RF power in both cases is close in magnitude ∼0.7 kW. Increasing the RF power injection by a factor of two (see Fig. 9) does not result in significant changes compared to the data in Fig. 8 discussed earlier. Accordingly, for a more detailed analysis, it is necessary to consider the RF wave propagation under these experimental conditions. This will be discussed in Sec. III C.

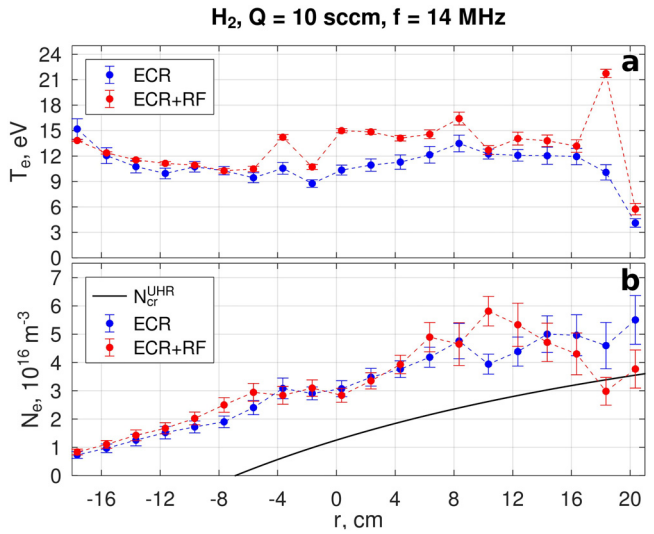

FIG. 8. Radial distribution of electron temperature T_e (a) and density N_e (b) for ECR discharge $P_{MW}(max) \approx 1.75$ kW and combined ECR+RF discharge $P_{MW}(max) \approx 2$ kW, $P_{RF}(max) \approx 0.7$ kW, f = 14 MHz (gas: H_2, continuous gas flow Q = 10 sccm, initial pressure $p_0 = 2.3 \times 10^{-2}$ Pa). Black solid lines (b) indicate density necessary to fulfill of the UHR condition.

C. Propagation of radio frequency waves in low magnetic fields

The dispersion equation for a cold plasma in a magnetic field is in the form of a bi-quadratic equation,[49–53]

$$AN_{\perp}^4 + BN_{\perp}^2 + C = 0, \quad (1)$$

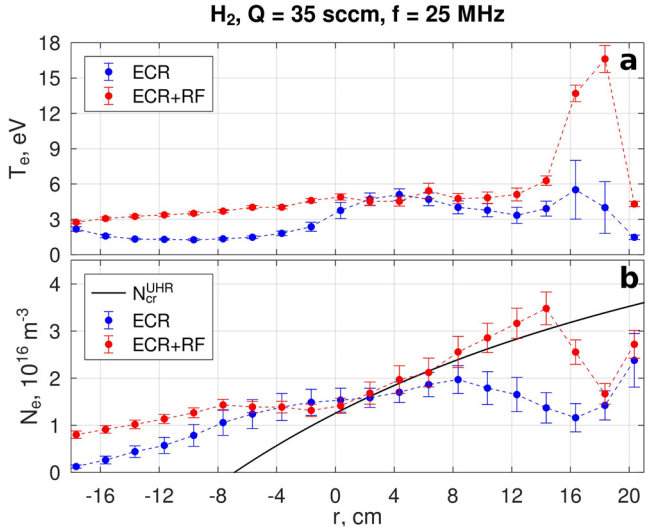

FIG. 7. Radial distribution of electron temperature T_e (a) and density N_e (b) for ECR discharge $P_{MW}(max) \approx 1.8$ kW and combined ECR+RF discharge $P_{MW}(max) \approx 1.8$ kW, $P_{RF}(max) \approx 0.75$ kW, f = 25 MHz (gas: H_2, continuous gas flow Q = 35 sccm, initial pressure $p_0 = 0.13$ Pa). Black solid lines (b) indicate density necessary to fulfill of the UHR condition.

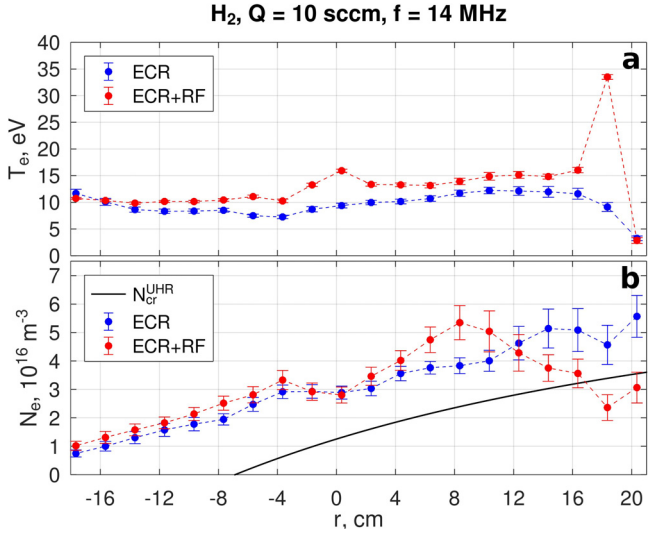

FIG. 9. Radial distribution of electron temperature T_e (a) and density N_e (b) for ECR discharge $P_{MW}(max) \approx 1.75$ kW and combined ECR+RF discharge $P_{MW}(max) \approx 2.2$ kW, $P_{RF}(max) \approx 1.4$ kW, f = 14 MHz (gas: H_2, continuous gas flow Q = 10 sccm, initial pressure $p_0 = 2.3 \times 10^{-2}$ Pa). Black solid lines (b) indicate density necessary to fulfill of the UHR condition.

where $N_\perp$ is perpendicular refractive indices ($N_\perp = k_\perp/k_0$, with $k_\perp$ as the perpendicular wavenumber and k_0 as the wavenumber in a vacuum), $A = S$, $B = [(N_{||} - S)(S + P) + D^2]$, and $C = P[(S - N_{||}^2)^2 - D^2]$, where S, P, and D are the Stix parameters.[49] The parallel refractive indices $N_{||} = k_{||}/k_0$, where $k_{||}$ is a parallel wavenumber.

The solution to Eq. (1) is

$$N_\perp^2 = \frac{-B \pm \sqrt{B^2 - 4AC}}{2A}. \quad (2)$$

In Eq. (2), the (+) sign should be chosen for the slow wave (SW) and the (−) sign is for the fast wave (FW). Equations (1) and (2) were used for calculations of squared perpendicular wave numbers for SW and FW. According to Ref. 51, the Fourier transform of the antenna current density for unity total current along a single-strap antenna can be written as

$$J_{ant} = \frac{\sin(k_{||} w)/2}{(k_{||} w)/2}, \quad (3)$$

where w is the width of the antenna strap. The normalized nominal power spectrum can be estimated as[54]

$$P_{norm} = J_{ant}^2(k_{||}). \quad (4)$$

The results of the calculation using formulas (3) and (4) are shown in Fig. 10. The maximum is at $k_{||} = 0$ m^{-1}, the first minima are $k_{||} \approx \pm 34.9$ m^{-1}; these values can also be estimated from the relation $k_{||} \sim \pi/w$.[55]

The wavelength and wave vector in vacuum are $\lambda_0 = 11.99$ m and $k_0 = 0.524$ m^{-1} for the frequency $f_{RF} = 25$ MHz. For the frequency $f_{RF} = 14$ MHz, the wavelength and wavenumber in vacuum are $\lambda_0 = 21.41$ m and $k_0 = 0.293$ m^{-1}, respectively.

The results of calculations of square perpendicular wave numbers of SW and FW at $B_0 = $ const and $k_{||} = $ const as a function of the hydrogen plasma density are presented in Fig. 11. Positive values of $\lg(|k^2{}_\perp|)\mathrm{sign}(k^2{}_\perp)$ correspond to propagating waves. The values of $\lg(|k^2{}_\perp|)\mathrm{sign}(k^2{}_\perp)$ less than 0 belong to evanescent regions. Although these data representation is visually easy to interpret, for $k^2{}_\perp < 1$, the value of $\lg(|k^2{}_\perp|)$ may have a negative sign for positive $k^2{}_\perp$, and so naturally $\lg(|k^2{}_\perp|)\mathrm{sign}(k^2{}_\perp)$. Also for $k^2{}_\perp = 0$, the value of $\lg(|k^2{}_\perp|)$ $= -\infty$. In these cases, we neglect these points and assign them a value equal to zero. This correction is necessary to avoid confusion with peaks that can be visually mistaken for resonances. At the same time, such a correction does not introduce inaccuracies.

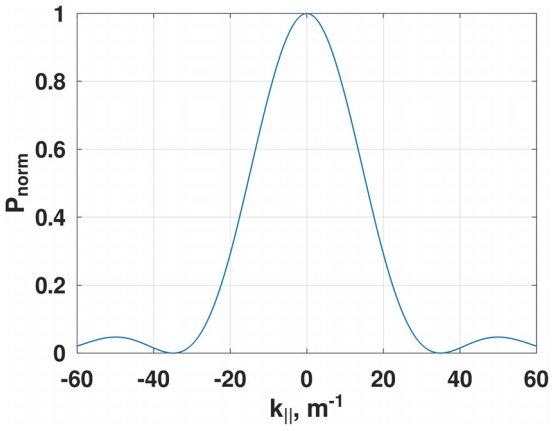

FIG. 10. The nominal power spectra of a single-strap antenna.

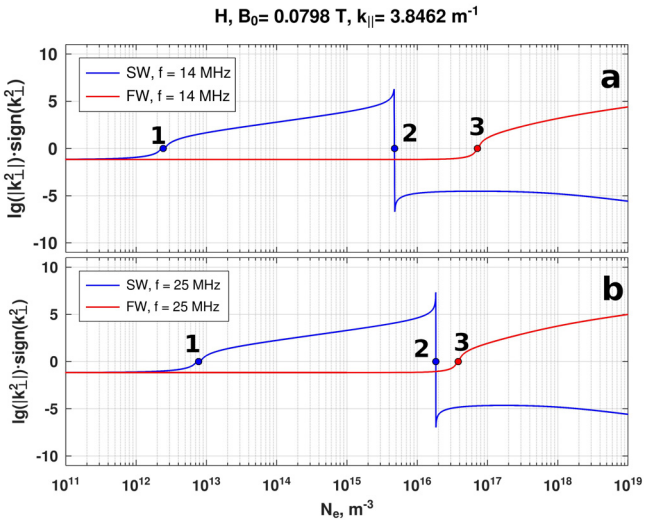

FIG. 11. The squared perpendicular wave numbers of SW and FW for frequency 14 MHz (a) and 25 MHz (b) as a function of the hydrogen plasma density. The points: (1) the SW critical density $n_{ec}^{(1)SW}$; (2) the SW critical density $n_{ec}^{(2)SW}$ (the lower hybrid resonance); (3) the FW critical density n_{ec}^{FW}.

In this case, when $\omega_{RF} > \omega_{ci}$, there are two points for SW. The first cutoff point (see Fig. 11, point 1), defined by the condition $k_{\perp,SW} = 0$, marks the density value above which SW propagation is possible, $|N_{||}| > 1$. The critical density at a given cutoff point $n_{ec}^{(1)SW}$ can be estimated from the relation $\omega_{RF}{}^2 = \omega_{pe}{}^2 + \omega_{pi}{}^2$, where ω_{pe} and ω_{pi} are the electron and ion plasma frequencies, respectively.[49] As can be seen from Fig. 11, the value of the critical density is higher at 25 MHz than at 14 MHz. For plasma production by RF discharge only, this cutoff characterizes the transition from the non-wave state to the state where slow wave propagation in the plasma is possible.[49,56] This is important for RF startup. In the experiments presented in this paper, the plasma was created by ECR discharge, and the density was significantly higher than $n_{ec}^{(1)SW}$. According to this, RF waves can propagate at the beginning of RF power injection into the plasma.

The second point (see Fig. 11, points 2) is determined by $k^2{}_{\perp,SW} \to \infty$, and the value of $n_{ec}^{(2)SW}$ from the lower hybrid resonance (LHR) condition $\omega_{RF}{}^2 = \omega_{LH}{}^2$.[49]

Above this density, SW cannot propagate. For a frequency of 25 MHz, the value of $n_{ec}^{(2)SW}$ is higher than for a frequency of 14 MHz (see Fig. 11). Since the magnetic field varies with the radius, the value of $n_{ec}^{(2)SW}$ also varies. However, in the case of the magnetic field values in the studied plasmas, $n_{ec}^{(2)SW}$ lies in a rather narrow range, $\approx (1.6\text{–}2.4) \times 10^{16}$ m^{-3} and $\approx (4.5\text{–}5.1) \times 10^{15}$ m^{-3} for 25 and 14 MHz, respectively.

In the case of FW, there is a cutoff point (see Fig. 11, points 3) under the condition $k_{\perp,FW} = 0$. The critical density n_{ec}^{FW} above which FW propagation is possible is determined by the relation $\omega_{pi}{}^2 = (N_{||}{}^2 - 1)\Omega_i(\omega_{RF} + \Omega_i)$[49] and depends on $N_{||}$ and $k_{||}$, respectively,

determined by the antenna spectrum. Based on the data shown in Fig. 10, the critical density for the FW has been calculated. Figure 12 shows the dependence of n_{ec}^{FW} as a function of $k_{||}$. It can be seen that the n_{ec}^{FW} values for 25 MHz are lower than those for 14 MHz. Accordingly, the simultaneous propagation of SW and FW will be possible for larger values of $k_{||}$ at 25 MHz. For example, Figs. 11 and 12 show that at 25 MHz, SW and FW can propagate simultaneously for $k_{||} < 2.5\ m^{-1}$. At 14 MHz, this situation is possible for $k_{||} < 1\ m^{-1}$. Note that in this case for FW there is no upper limit to the plasma density above which propagation is not possible. It is also clear from Figs. 6 and 12 that FW will propagate if the plasma density exceeds the critical density for L-hand polarized microwaves. Accordingly, higher densities can be achieved with an ECR+RF discharge than with an ECR discharge.

The analysis of SW and FW propagation for the conditions of these experiments gives only a general picture of the wave propagation conditions. Naturally, $k^2_{\perp,SW}$ and $k^2_{\perp,FW}$ depend on the plasma density and the magnetic field. These vary along the radius in these experiments. Therefore, the square wave numbers of SW and FW are calculated taking into account the radial distribution of the magnetic field and the plasma density observed in the experiments. The magnitude of the magnetic field along the radius was calculated from the equation presented in Sec. III A. Earlier in Ref. 37, an analytical expression was used to approximate the density. This gives the correct general form of the density distribution. However, this function only allowed a more accurate approximation of some small regions of the distribution. Therefore, the experimental density values were approximated by a fifteenth order polynomial function. The results of the calculations are shown in Figs. 13 and 14.

The Figures 13(a) and 13(b) characterize B_0, N_e, and $k^2_{\perp}$ at the initial stage of RF injection at 25 MHz into the ECR discharge plasma when the plasma density distribution has not yet changed. It can be seen [see Fig. 13(b)] that the SW can start propagation at $r \sim 20$ cm into the HFS region. At the point $r \sim 20$ cm, the plasma density is

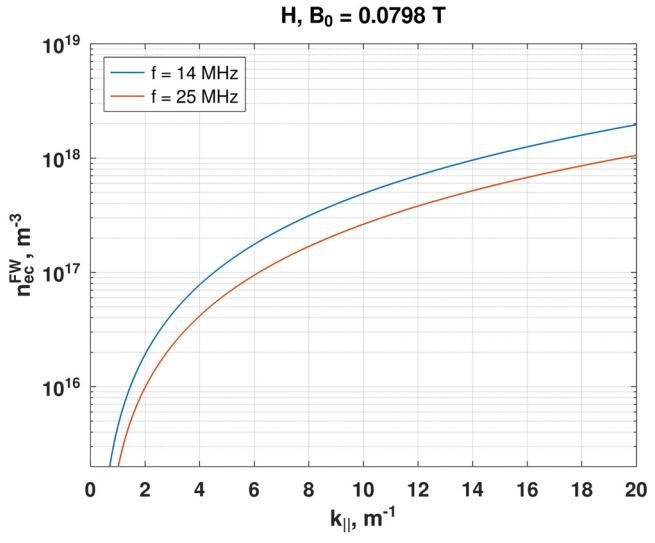

FIG. 12. The dependence of FW critical density n_{ec}^{FW} as a function of the parallel $k_{||}$ wavenumber for frequencies of 14 and 25 MHz.

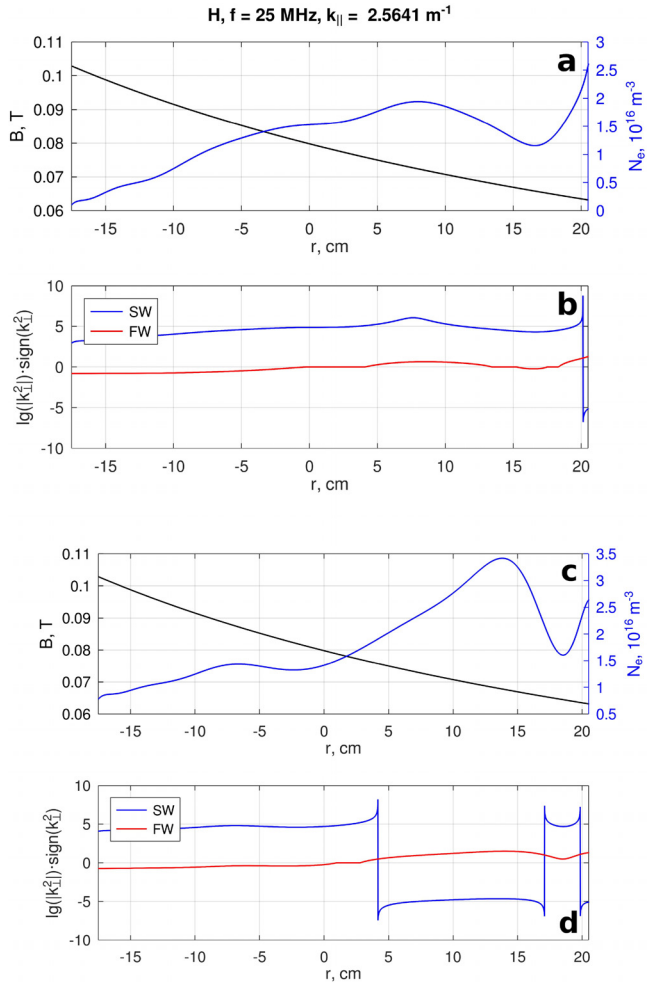

FIG. 13. Radial distribution of magnetic field in the equatorial plane, and plasma density (a) and (c). The squared perpendicular wave numbers of SW and FW for frequency 25 MHz in hydrogen plasma (b) and (d). The distributions of plasma density for ECR discharge (a) and ECR+RF discharge (c), are data approximation from Fig. 7(b).

equal to $n_{ec}^{(2)SW}$, and the condition for LHR is satisfied. For FW, the situation is different. FW propagation is possible for $k_{||} < 1\ m^{-1}$. As $k_{||}$ increases, FW can only propagate in some regions, e.g., $r \sim 4$–13 cm, as can be seen from Fig. 13(b). For higher values of $k_{||} > 4\ m^{-1}$, FW cannot propagate. In the case of the quasi-stationary stage for ECR+RF discharge [see Figs. 13(c) and 13(d)], the density distribution has changed compared to the ECR discharge [see Figs. 13(a), 13(c), and 7(b)], and the conditions for wave propagation have changed accordingly. For SW, three points $r \sim 4.2$, 17.1, and 19.9 cm are observed where the condition for LHR is satisfied. In the region $r \sim 4.2$–17.1 cm, SW does not propagate. However, FW can propagate. As in the previous case, FW cannot propagate at $k_{||} > 4\ m^{-1}$.

The case of RF injection at 14 MHz into the ECR discharge plasma is shown in Figs. 14(a) and 14(b). In the considered case, the initial plasma density along the radius is higher than $n_{ec}^{(2)SW}$, respectively, SW does not propagate. Only FW can propagate.

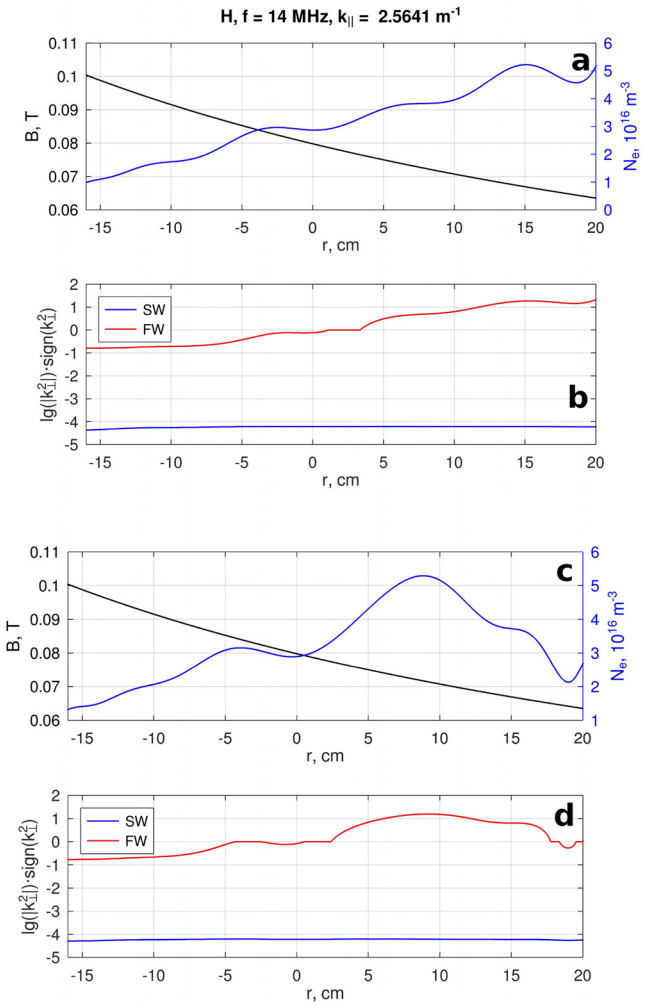

FIG. 14. Radial distribution of magnetic field in the equatorial plane, and plasma density (a) and (c). The squared perpendicular wave numbers of SW and FW for the frequency 14 MHz in hydrogen plasma (b) and (d). The distributions of plasma density for ECR discharge (a) and ECR+RF discharge (c) are data approximation from Fig. 9(b).

Similar to the previously considered cases, FW propagation is possible at $k_{||} < 4\ m^{-1}$. For higher values of $k_{||}$, FW propagation is not possible. Although the radial density distribution changes in the ECR+RF discharge relative to the ECR discharge [see Figs. 14(a), 14(c), and 9(b)], the general picture of RF wave propagation does not change. Only FW can propagate at low values of $k_{||}$.

It follows from the analysis that the injection of additional RF plasma power leads to changes in plasma parameters, which in turn leads to changes in microwave propagation conditions (see Sec. III B). However, depending on the plasma density and the RF plasma frequency, it can also lead to significant changes in the SW and FW propagation conditions in the plasma. As a result, there is a complex picture of mutual influence on the propagation of microwave and RF plasma waves associated with changes in plasma parameters, which in turn are related to the conditions of wave propagation and absorption in the plasma. It can be seen from Figs. 7(a) and 13(d) that the possibility of wave propagation in both LFS and HFS can lead to electron heating in these areas, which can be seen in Fig. 7(a). In the case of Fig. 14(d), only the FW can propagate in the LFS and the central region. As a result, a significant temperature increase is observed in the LFS, while there is almost no T_e change in the HFS [see Fig. 9(a)]. Nevertheless, the injection of additional RF power is an additional lever to change both the plasma parameters considered in Sec. III B and the neutral particle flux. This issue is considered in the next paragraph.

D. Neutral particle fluxes

When using ECR and ECR+RF discharges for wall conditioning, one of the important parameters is the flux of neutral atoms from the plasma. ToF NPA has been used to measure the flux of fast neutral hydrogen atoms from the plasma of ECR and ECR+RF discharges.[36,41] The ToF NPA measurement technique is described in detail in Ref. 36. The experiments are performed under the same initial conditions, magnetic field values and scenarios as described in detail in Sec. III A. The RF frequency was 25 MHz in all experiments.

Figure 15 shows that the injection of additional RF power into the ECR discharge plasma leads to an increase in the neutral flux of atomic hydrogen from the plasma. The injection of small RF power ≈ 0.26 kW relative to microwave power ≈ 1.7 kW leads to an increase in the H^0 flux by a factor of $\sim$2.5. In ECR+RF discharge at RF power $P_{RF} \approx 1.57$ kW, the H^0 flux increases by a factor of $\sim$9.3 compared to ECR discharge. Earlier, in the first experiments at TOMAS, the H^0 flux from the ECR+RF discharge plasma was also observed to be larger than that from the ECR discharge.[34] This may be due to an increase in the plasma density and a corresponding change in the density profile in the ECR+RF discharge compared to the ECR discharge. This is observed in both, hydrogen (see Figs. 3 and 7, also Refs. 37 and 57) and helium, discharges.[37] As a result, more ions participate in the charge exchange processes on neutral hydrogen atoms and molecules.

Differential flux spectra of neutrals from the ECR discharge plasma are averaged for a series of five measurements and are shown

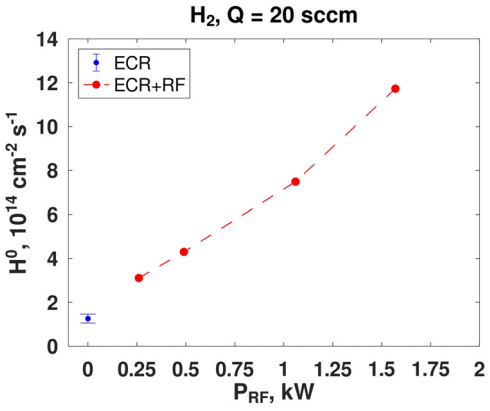

FIG. 15. Dependence of the atomic hydrogen neutral flux on RF power P_{RF} [gas: H_2, continuous gas flow Q = 20 sccm, initial pressure $p_0 = 6 \times 10^{-2}$ Pa, ECR discharge $P_{MW}(max) \approx 1.7$ kW, combined ECR+RF discharge f = 25 MHz].

in Fig. 16. Each series consists of more than 20 pulses. A fitting of several distribution functions to the experimental points is carried out. In the case of Maxwell–Boltzmann (M-B) distributions, the fitting is performed for two values of the conventionally cold T_c and hot T_h temperatures. When using the M-B distribution with $T_c = 18$ eV, the energy range up to ~50 eV is approximately characterized. When using the M-B distribution with $T_h = 35$ eV, the energy region above 50 eV is approximately characterized. It can be seen from Fig. 16 that the distribution is non-Maxwellian. In this case, the bimodal Maxwell–Boltzmann distribution can be used. This is a superposition of two M-B distributions at different temperatures.[58,59] It can be seen in Fig. 16 that using the bimodal M-B with $T_c = 18$ eV (73%) and $T_h = 50$ eV (27%) satisfactorily describes the experimentally observed distribution. The kappa distribution is also used to fit non-Maxwellian distributions.[56,58,59] For comparison, Fig. 16 also shows the fit using the kappa distribution for $T_k = 10$ eV and $\kappa = 4.6$. It can be seen that the kappa distribution satisfactorily describes the experimental distribution at energies higher than ~100 eV.

In the ECR+RF discharge, not only the H^0 flux increases but also the differential flux spectra of the neutrals from the plasma change compared to the ECR discharge, as can be seen in Fig. 17. At low RF power ≈0.26 kW, the flux of neutrals increases with energy up to ~85 eV. In the region above ~85 eV, there is almost no change. In this case, bimodal M-B with $T_c = 18$ eV (90%) and $T_h = 50$ eV (10%) should be used. Correspondingly, the fraction of conventionally cold T_c particles increases. This can be related to the change in density and the change in the plasma density profile. Further increase in the RF power up to ≈0.49 kW leads to an increase in the flux of neutrals with energy up to ~130 eV practically without changing the distribution function. In the case of RF power ≈1.57 kW, an increase in the flux of neutrals is observed over almost the whole energy range (see Fig. 17). The bimodal M-B fit gives the values of $T_c = 23$ eV (83%) and $T_h = 45$ eV (17%). Thus, the injection of additional RF power into the ECR discharge plasma leads not only to an increase in the atomic hydrogen flux but also to the change in the energy distribution function.

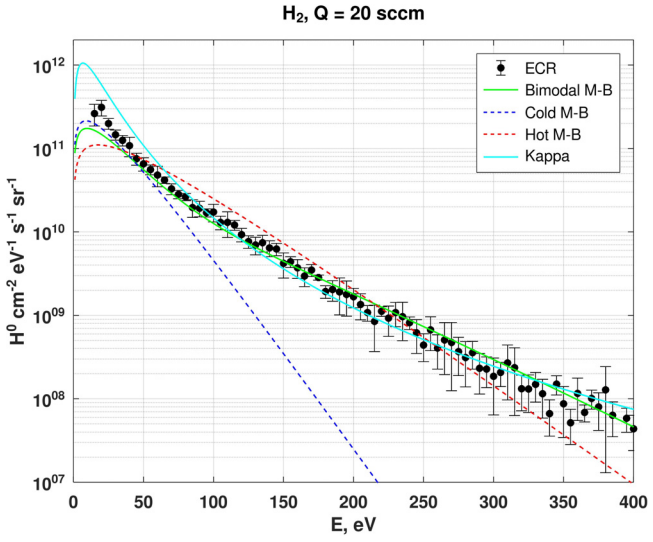

FIG. 16. Differential flux spectra of neutrals for ECR discharge. ECR experimental data. See the experimental conditions in the caption of Fig. 15. Distribution: bimodal M-B for $T_c = 18$ eV (73%) and $T_h = 50$ eV (27%); cold M-B for $T_c = 18$ eV; hot M-B for $T_h = 35$ eV; Kappa for $T_k = 10$ eV and $\kappa = 4.6$.

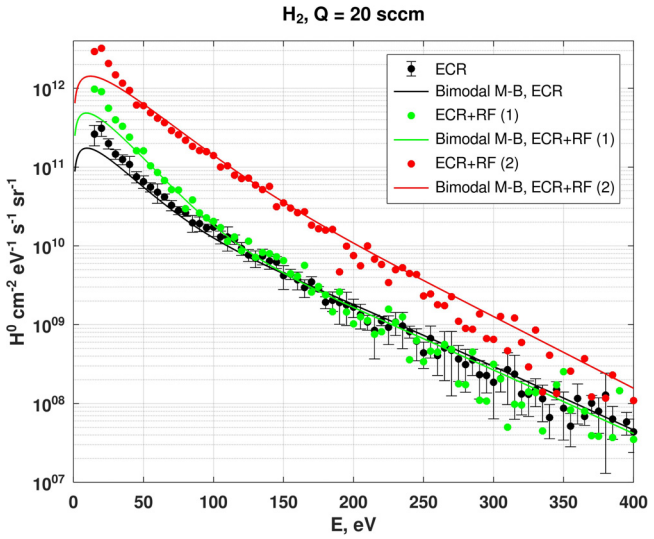

FIG. 17. Comparison of differential flux spectra of neutrals for ECR and ECR+RF discharges. The experimental data: ECR, ECR+RF (1) for $P_{RF} \approx 0.26$ kW, ECR+RF (2) for $P_{RF} \approx 1.57$ kW. See the experimental conditions in the caption of Fig. 15. Distribution: bimodal M-B, ECR for $T_c = 18$ eV (73%) and $T_h = 50$ eV (27%); bimodal M-B, ECR+RF (1) for $T_c = 18$ eV (90%) and $T_h = 50$ eV (10%); bimodal M-B, ECR+RF (2) for $T_c = 23$ eV (83%) and $T_h = 45$ eV (17%).

IV. CONCLUSION

In the studies of the combined ECR+RF discharge in TOMAS, the plasma parameters are observed to change when additional RF power is injected into the ECR discharge and the combined ECR+RF discharge is realized. It is possible to achieve higher electron temperature and plasma density than in ECR discharge. A similar situation was previously observed in helium[35] and hydrogen[37] experiments. The maximum plasma density of up to $\approx 6 \times 10^{16}$ m^{-3} and electron temperature of up to 35 eV are observed in hydrogen plasma of the combined ECR+RF discharge. In previous experiments, maximum plasma densities up to $\approx 4.5 \times 10^{16}$ m^{-3} and electron temperatures up to 24 eV were observed,[37] which are nearly the values obtained in this work. Changes in plasma parameters lead to changes in microwave propagation and absorption conditions. As a result, there is a complex picture of mutual influence on the propagation of microwaves and RF waves associated with changes in plasma parameters, which, in turn, are related to the conditions of their propagation and absorption in the plasma. The analysis of RF wave propagation in a weak magnetic field has shown that depending on RF frequency and experimental conditions, such as radial distribution of plasma density and magnetic field, there can be several cases: only SW propagation, simultaneously SW and FW propagation, and when only FW can propagate. Furthermore, FW can only propagate at small values of $k_{||} < 4$ m^{-1}. In the regions where the propagation of these waves is possible, an increase in the temperature of the electrons is observed. The injection of additional RF power is an additional lever to change both the plasma parameters

and the flux of neutral particles. The injection of small RF power ≈ 0.26 kW relative to microwave power ≈ 1.7 kW leads to an increase in the H^0 flux by a factor of ∼2.5. In ECR+RF discharge at RF power $P_{RF} \approx 1.57$ kW, the H^0 flux increases by a factor of ∼9.3 compared to the ECR discharge. The injection of additional RF power into the ECR discharge plasma leads not only to an increase in the atomic hydrogen flux but also to a change in the energy distribution function. The possibility of controlling the fluxes and energies of the particles leaving the plasma volume is important for approaching the conditions necessary to study the plasma–surface interaction during wall conditioning and fusion edge plasma. The presence of both ECR and RF systems in large experimental fusion devices makes it possible to use them for the realization of the combined discharge.

ACKNOWLEDGMENTS

This work has been carried out within the framework of the EUROfusion Consortium, funded by the European Union via the Euratom Research and Training Programme (Grant Agreement No. 101052200—EUROfusion). Views and opinions expressed are, however, those of the author(s) only and do not necessarily reflect those of the European Union or the European Commission. Neither the European Union nor the European Commission can be held responsible for them.

The views and opinions expressed herein do not necessarily reflect those of the ITER Organization.

This work was supported by the National Research Foundation of Ukraine under Grant No. 2022.02/0036 as part of the "Cambridge—NRFU 2022," which provides individual research (developments) grants for researchers in Ukraine (supported by the University of Cambridge, UK).

AUTHOR DECLARATIONS

Conflict of Interest

The authors have no conflicts to disclose.

Author Contributions

Yu. Kovtun: Conceptualization (lead); Data curation (equal); Formal analysis (equal); Investigation (equal); Methodology (equal); Validation (equal); Visualization (lead); Writing – original draft (lead); Writing – review & editing (lead). **T. Wauters:** Formal analysis (equal); Investigation (equal); Methodology (equal); Writing – original draft (supporting); Writing – review & editing (supporting). **A. Goriaev:** Data curation (equal); Formal analysis (equal); Investigation (equal); Methodology (equal); Writing – original draft (supporting); Writing – review & editing (supporting). **L. Dittrich:** Data curation (equal); Formal analysis (equal); Investigation (equal); Methodology (equal). **L. D. López-Rodríguez:** Data curation (equal); Formal analysis (equal); Investigation (equal); Methodology (equal). **K. Crombé:** Data curation (equal); Investigation (equal); Methodology (equal). **S. Moon:** Investigation (equal); Methodology (equal). **P. Petersson:** Investigation (equal); Methodology (equal). **J. Buermans:** Investigation (equal); Methodology (equal). **S. Möller:** Investigation (equal); Methodology (equal). **S. Brezinsek:** Project administration (equal); Supervision (equal).

DATA AVAILABILITY

The data that support the findings of this study are available from the corresponding author upon reasonable request.

REFERENCES

[1]G. Guest, *Electron Cyclotron Heating of Plasmas* (WILEY-VCH Verlag GmbH & Co. KgaA., 2009).
[2]J.-M. Noterdaeme, "Fifty years of progress in ICRF, from first experiments on the model C stellarator to the design of an ICRF system for DEMO," AIP Conf. Proc. **2254**, 020001 (2020).
[3]M. Endler, J. Baldzuhn, C. D. Beidler, H.-S. Bosch, S. Bozhenkov, B. Buttenschön, A. Dinklage, J. Fellinger, Y. Feng, G. Fuchert *et al.*, "Wendelstein 7-X on the path to long-pulse high-performance operation," Fusion Eng. Des. **167**, 112381 (2021).
[4]Y. O. Kazakov, J. Ongena, J. C. Wright, S. J. Wukitch, V. Bobkov, J. Garcia, V. G. Kiptily, M. J. Mantsinen, M. Nocente, M. Schneide *et al.*, "Physics and applications of three-ion ICRF scenarios for fusion research," Phys. Plasmas **28**(2), 020501 (2021).
[5]J. Hillairet, "Review on recent progress in ion cyclotron range of frequency systems, experiments and modelling for magnetic confnement fusion," Rev. Mod. Plasma Phys. **7**(1), 16 (2023).
[6]E de La Cal and E. Gauthier, "Review on recent progress in ion cyclotron range of frequency systems, experiments and modelling for magnetic confnement fusion," Plasma Phys. Controlled Fusion **47**(2), 197–218 (2005).
[7]T. Wauters, D. Borodin, R. Brakel, S. Brezinsek, K. J. Brunner, J. Buermans, S. Coda, A. Dinklage, D. Douai, O. Ford *et al.*, "Wall conditioning in fusion devices with superconducting coils," Plasma Phys. Controlled Fusion **62**(3), 034002 (2020).
[8]Y. Kovtun, T. Wauters, D. Matveev, R. Bisson, I. Jepu, S. Brezinsek, I. Coffey, E. Delabie, A. Boboc, T. Dittmar *et al.*, "Comparison of ion cyclotron wall conditioning discharges in hydrogen and helium in JET," Nucl. Mater. Energy **37**, 101521 (2023).
[9]A. Lyssoivan, D. A. Hartmann, J.-M. Noterdaeme, R. Koch, V. Bobkov, T. Blackman, F. Braun, M. Cox, P. de Vries, H. G. Esser *et al.*, "Development of ICRF wall conditioning technique on divertor-type tokamaks ASDEX Upgrade and JET," J. Nucl. Mater. **337–339**, 456–460 (2005).
[10]D. Douai, A. Lyssoivan, V. Philipps, V. Rohde, T. Wauters, T. Blackman, V. Bobkov, S. Brémond, S. Brezinsek, F. Clairet *et al.*, "Recent results on Ion Cyclotron Wall Conditioning in mid and large size tokamaks," J. Nucl. Mater. **415**(1), S1021–S1028 (2011).
[11]A. Lyssoivan, G. Sergienko, V. Rohde, V. Philipps, G. van Wassenhove, M. Vervier, V. Bobkov, J. Harhausen, R. Koch, J.-M. Noterdaeme *et al.*, "Influence of toroidal and vertical magnetic fields on Ion Cyclotron Wall Conditioning in tokamaks," J. Nucl. Mater. **390–391**, 907–910 (2009).
[12]V. E. Moiseenko, V. L. Berezhnyj, V. N. Bondarenko, P. Y. Burchenko, F. Castejón, V. V. Chechkin, V. Y. Chernyshenko, M. B. Dreval, I. E. Garkusha, G. P. Glazunov *et al.*, "RF plasma production and heating below ioncyclotron frequencies in Uragan torsatrons," Nucl. Fusion **51**(8), 083036 (2011).
[13]A. V. Lozin, V. E. Moiseenko, L. I. Grigor'eva, M. M. Kozulya, A. E. Kulaga, A. I. Lysoivan, Y. K. Mironov, R. O. Pavlichenko, V. S. Romanov, V. Y. Chernyshenko *et al.*, "Cleaning of inner vacuum surfaces in the Uragan-3M facility by radio-frequency discharges," Plasma Phys. Rep. **39**, 624–631 (2013).
[14]A. V. Lozin, Y. V. Kovtun, V. E. Moiseenko, S. M. Maznichenko, M. M. Kozulia, V. B. Korovin, A. N. Shapoval, E. D. Kramskoy, R. O. Pavlichenko, N. V. Zamanov *et al.*, "Two-strap RF antenna in URAGAN-2M stellarator," Probl. At. Sci. Technol. Ser.: Plasma Phys. **6**(26), 10–14 (2020).
[15]Y. V. Kovtun, V. E. Moiseenko, A. V. Lozin, M. M. Kozulya, A. N. Shapoval, R. O. Pavlichenko, N. V. Zamanov, D. I. Baron, V. N. Bondarenko, S. M. Maznichenko *et al.*, "Radio frequency wall conditioning discharges at low magnetic fields in Uragan-2M stellarator," in *48th EPS Conference on Plasma Physics, 27 June–1 July 2022, Online, Maastricht, Netherlands, ECA* (EPS, 2022), Vol. 46A, p. O2.J503.
[16]A. Goriaev, T. Wauters, R. Brakel, S. Brezinsek, A. Dinklage, J. Fellinger, H. Grote, D. Moseev, S. Sereda, O. Volzke, and W7-X. team, "Wall conditioning at

the Wendelstein 7-X stellarator operating with a graphite divertor," Phys. Scr. **2020**(T171), 014063.
[17]T. Wauters, R. Brakel, S. Brezinsek, A. Dinklage, A. Goriaev, H. Laqua, S. Marsen, D. Moseev, T. Stange, G. Schlisio *et al.*, "Wall conditioning by ECRH discharges and He-GDC in the limiter phase of Wendelstein 7-X," Nucl. Fusion **58**(6), 066013 (2018).
[18]Y. Sakamoto, Y. Ishibe, K. Yano, H. Oyama, Y. Tanaka, N. Fujisawa, Y. Matsuzaki, N. Suzuki, K. Maeno, T. Yamamoto, and K. Yokokura, "Electron cyclotron resonance discharge cleaning of JFT-2 Tokamak (Jaeri)," J. Nucl. Mater. **93–94**, 333–337 (1980).
[19]R. T. Nachtrieb, B. L. LaBombard, J. L. Terry, J. C. Reardon, W. L. Rowan, and W. R. Wampler, "Electron cyclotron discharge cleaning (ECDC) experiments on Alcator C-Mod," J. Nucl. Mater. **266–269**, 896–900 (1999).
[20]Y. W. Yu, X. Gao, J. S. Hu, J. G. Li, J. F. Shan, and The HT-7 Team, "ECR discharge cleaning and followed He GDC on HT-7 tokamak," J. Nucl. Mater. **390–391**, 1051–1054 (2009).
[21]F. Deeba, A. Qayyum, M. U. Naseer, and S. Hussain, "Optical actinometric measurements of nitrogen impurity in Ar/He microwave discharge during wall cleaning of MT-I spherical tokamak," Vacuum **182**, 109672 (2020).
[22]Y. A. Lebedev, "Microwave discharges at low pressures and peculiarities of the processes in strongly non-uniform plasma," Plasma Sources Sci. Technol. **24**(5), 053001 (2015).
[23]Yu. Kovtun, K. Nagasaki, S. Kobayashi, T. Minami, S. Kado, S. Ohshima, Y. Nakamura, A. Ishizawa, S. Konoshima, T. Mizuuchi *et al.*, "Non resonant microwave discharge start up in Heliotron J," Probl. At. Sci. Technol., Ser.: Plasma Phys. **1**, 3–8 (2023).
[24]S. Kobayashi, K. Nagasaki, K. Hada, T. Stange, H. Okada, T. Minami, S. Kado, S. Ohshima, K. Tokuhara, Y. Nakamura *et al.*, "Role of pre-ionization in NBI plasma start-up of Heliotron J using non-resonant microwave heating," Nucl. Fusion **61**(11), 116009 (2021).
[25]S. Kobayashi, K. Nagasaki, T. Stange, T. Mizuuchi, H. Okada, T. Minami, S. Kado, S. Yamamoto, S. Ohshima, K. Hada *et al.*, "Study of seed plasma generation for NBI plasma start-up using non-resonant microwave launch in Heliotron J," Plasma Phys. Controlled Fusion **62**(6), 065009 (2020).
[26]S. Kobayashi, K. Nagasaki, S. Yamamoto, K. Sakamoto, T. Mizuuchi, H. Okada, T. Minami, K. Hanatani, Y. Nakamura, S. Konoshima *et al.*, "Plasma startup using neutral beam injection assisted by 2.45 GHz microwaves in Heliotron J," Nucl. Fusion **51**(6), 062002 (2011).
[27]M. Otte, H. P. Laqua, S. Marsen, Y. Podoba, J. Preinhaelter, T. Stange, J. Urban, F. Wagner, and D. Zhang, "Overdense plasma operation in the WEGA Stellarator," Contrib. Plasma Phys. **50**(8), 785–789 (2010).
[28]A. Köhn-Seemann, G. Birkenmeier, P. Diez, E. Holzhauer, S. Merli, M. Ramisch, G. Sichardt, and U. Stroth, "Plasma electron acceleration in a non-resonant microwave heating scheme below the electron cyclotron frequency," New J. Phys. **24**, 063024 (2022).
[29]A. Lyssoivan, R. Koch, E. Gauthier, F. Hoekzema, A. Messiaen, V. Philipps, M. Vervier, E. Westerhof, R. Weynants, D. Van Eester *et al.*, "ICRF/ECR plasma production for wall conditioning in TEXTOR-94," AIP Conf. Proc. **595**, 146–149 (2001).
[30]E. Gauthier, A. Lyssoivan, H. G. Esser, M. Freisinger, F. Hoekzema, P. Hüttemann, J. Ihde, R. Koch, V. Philipps, H. Reimer *et al.*, "ECR and ICRF conditioning discharges comparison in TEXTOR-94," in *28th EPS Conference Controlled Fusion and Plasma Physics, Madeira* (EPS, 2001), p. P5.094.
[31]Y. H. Lee, J. E. Heidenreich III, and G. Fortuno, "Plasma characterization of an electron cyclotron resonance–radio-frequency hybrid plasma reactor," J. Vac. Sci. Technol. A **7**(3), 903–907 (1989).
[32]Y. H. Lee, K. K. Chan, and M. J. Brady, "Plasma enhanced chemical vapor deposition of TiO_2 in microwave-radio frequency hybrid plasma reactor," J. Vac. Sci. Technol., A **13**(3), 596–601 (1995).
[33]J. Hong, A. Granier, C. Leteinturier, M.-C. Peignon, and G. Turban, "Measurements of rf bias effect in a dual electron cyclotron resonance-rf methane plasma using the Langmuir probe method," J. Vac. Sci. Technol., A **18**(2), 497–502 (2000).
[34]L. Wang, B. Ke, T. L. Ni, F. Ding, M. D. Chen, X. D. Zhu, H. Y. Zhou, and X. H. Wen, "Role of bias frequency in a dual electron cyclotron resonance-radio-frequency hybrid plasma," Vacuum **84**(2), 348–351 (2009).
[35]Yu. Kovtun, T. Wauters, A. Goriaev, S. Möller, D. López-Rodríguez, K. Crombé, S. Brezinsek, A. Dinklage, D. Nicolai, Ch. Linsmeier *et al.*, "Comparative analysis of the plasma parameters of ECR and combined ECR + RF discharges in the TOMAS plasma facility," Plasma Phys. Controlled Fusion **63**(12), 125023 (2021).
[36]S. Moon, P. Petersson, P. Brunsell, M. Rubel, A. Goriaev, R. Ragona, S. Möller, S. Brezinsek, D. Nicolai, C. Linsmeier *et al.*, "Characterization of neutral particle fluxes from ICWC and ECWC plasmas in the TOMAS facility," Phys. Scr. **96**(12), 124025 (2021).
[37]Yu. Kovtun, T. Wauters, A. Goriaev, D. López-Rodríguez, K. Crombé, L. Dittrich, P. Petersson, S. Moon, S. Möller, J. Buermans, and S. Brezinsek, "Measurement of hydrogen plasma parameters of the combined ECR+RF discharge in the TOMAS facility," AIP Conf. Proc. **2984**(1), 110001 (2023).
[38]Yu. Kovtun, A. Goriaev, D. López-Rodríguez, L. Dittrich, P. Petersson, S. Moon, T. Wauters, K. Crombé, S. Möller, J. Buermans *et al.*, "Overview of TOMAS plasma diagnostics," J. Instrum. **18**, C02034 (2023).
[39]J. G. Bak, Y. S. Oh, H. S. Kim, S. H. Hahn, S. W. Yoon, Y. M. Jeon, W. W. Xiao, W. H. Ko, W. C. Kim, J. G. Kwak *et al.*, "Electric probe measurements at edge region during H-mode discharges in KSTAR," Contrib. Plasma Phys. **53**(1), 69–74 (2013).
[40]H. B. Störk, J. Winter, J. Ihde, H. G. Esser, H. Reimer, and M. Freisinger, "TOMAS—A toroidal magnetized plasma facility for studying wall conditioning of future fusion devices," Fusion Sci. Technol. **39**(1), 54–60 (2001).
[41]A. Goriaev, T. Wauters, S. Möller, R. Brakel, S. Brezinsek, J. Buermans, K. Crombé, A. Dinklage, R. Habrichs, D. Höschen *et al.*, "The upgraded TOMAS device: A toroidal plasma facility for wall conditioning, plasma production, and plasma–surface interaction studies," Rev. Sci. Instrum. **92**(2), 023506 (2021).
[42]S.-L. Chen and T. Sekiguchi, "Instantaneous direct-display system of plasma parameters by means of triple probe," J. Appl. Phys. **36**(8), 2363–2375 (1965).
[43]K. Crombé, J. Buermans, D. Castaño-Bardawil, A. Goriaev, D. López-Rodríguez, M. Verstraeten, L. Dittrich, Yu. Kovtun, S. Möller, J. Ongena, P. Petersson, and T. Wauters, "Radio frequency plasma production on the TOMAS device," AIP Conf. Proc. **2984**, 040005 (2023).
[44]J. E. Sansonetti and W. C. Martin, "Handbook of basic atomic spectroscopic data," J. Phys. Chem. Ref. Data **34**(4), 1559–2259 (2005).
[45]K. C. Hammond, R. R. Diaz-Pacheco, A. Köhn, F. A. Volpe, and Y. Wei, "Overdense microwave plasma heating in the CNT stellarator," Plasma Phys. Controlled Fusion **60**(2), 025022 (2018).
[46]J. Buermans, K. Crombé, L. Dittrich, A. Goriaev, Y. Kovtun, S. Möller, D. López-Rodríguez, P. Petersson, M. Verstraeten, and T. Wauters, "X-mode electron cyclotron heating scenarios beyond the cut-off densit," AIP Conf. Proc. **2984**, 110003 (2023).
[47]J. Buermans, K. Crombé, L. Dittrich, A. Goriaev, Y. Kovtun, D. López-Rodríguez, S. Möller, P. Petersson, and M. Verstraeten, "Triple Langmuir probe calibration in TOMAS ECRH plasma," AIP Adv. **13**(5), 055125 (2023).
[48]J. Buermans, A. Adriaens, S. Brezinsek, K. Crombé, N. Desmet, L. Dittrich, A. Goriaev, Y. Kovtun, L. D. López-Rodríguez, P. Petersson, and M. Van Schoor, "Characterization of ECRH plasmas in TOMAS," Phys. Plasmas **31**(5), 052510 (2024).
[49]A. Lyssoivan, D. Douai, R. Koch, J. Ongena, V. Philipps, F. C. Schüller, D. Van Eester, T. Wauters, T. Blackman, V. Bobkov *et al.*, "Simulation of ITER full-field ICWC scenario in JET: RF physics aspects," Plasma Phys. Controlled Fusion **54**(7), 074014 (2012).
[50]T. H. Stix, *Waves in Plasmas* (Springer-Verlag, New York, 1992).
[51]A. V. Longinov and K. N. Stepanov, *High-Frequency Plasma Heating*, edited by A. G. Litvak (AIP, New York, 1992), pp. 93–238.
[52]K. Crombé and D. Van Eester, "Parameter study of ICRH wave propagation in IShTAR," J. Plasma Phys. **82**(2), 905820203 (2016).
[53]M. Usoltceva, R. Ochoukov, W. Tierens, A. Kostic, K. Crombé, S. Heuraux, and J.-M. Noterdaeme, "Simulation of the ion cyclotron range of frequencies slow wave and the lower hybrid resonance in 3D in RAPLICASOL," Plasma Phys. Controlled Fusion **61**(11), 115011 (2019).
[54]A. K. Dash and A. K. Chattopadhyay, "Estimation of power transmission of fast wave in ICRF range through tokamak plasma edge with the help of reflection coefficient," Fusion Sci. Technol. **77**(1), 67–75 (2021).
[55]R. Koch, "The coupling of electromagnetic power to plasmas," Fusion Sci. Technol. **53**(2T), 184–193 (2008).

[56]M. Tripský, T. Wauters, A. Lyssoivan, V. Bobkov, P. A. Schneider, I. Stepanov, D. Douai, D. Van Eester, J.-M. Noterdaeme, M. Van Schoor *et al.*, "A PIC-MCC code RFdinity1d for simulation of discharge initiation by ICRF antenna," Nucl. Fusion **57**(12), 126043 (2017).
[57]D. López-Rodríguez, K. Crombé, A. Goriaev, J. Buermans, A. Adriaens, Y. Kovtun, L. Dittrich, P. Petersson, T. Wauters, and S. Brezinsek, "Characterization of plasma parameters and neutral particles in ERCH and radio frequency discharges in the TOMAS device," in *25th Topical Conference on High Temperature Plasma Diagnostics HTPD, 21–25 April 2024, Asheville, North Carolina* (AIP Publishing LLC, 2024), p. 2.2.21.
[58]B. I. Squarer, C. Presilla, and R. Onofrio, "Enhancement of fusion reactivities using non-Maxwellian energy distributions," Phys. Rev. E **109**(2), 025207 (2024).
[59]D. Vrinceanu, R. Onofrio, and H. R. Sadeghpour, "Non-Maxwellian rate coefficients for electron and ion collisions in Rydberg plasmas: Implications for excitation and ionization," J. Plasma Phys. **86**(3), 845860301 (2020).